



OPEN

# Characterisation of CaCO<sub>3</sub> phases during strain-specific ureolytic precipitation

Alexandra Clarà Saracho<sup>1</sup>✉, Stuart K. Haigh<sup>1</sup>, Toshiro Hata<sup>2</sup>, Kenichi Soga<sup>3</sup>, Stefan Farsang<sup>4</sup>, Simon A. T. Redfern<sup>5</sup> & Ewa Marek<sup>1</sup>

Numerous microbial species can selectively precipitate mineral carbonates with enhanced mechanical properties, however, understanding exactly how they achieve this control represents a major challenge in the field of biomineralisation. We have studied microbial induced calcium carbonate (CaCO<sub>3</sub>) precipitation (MICP) in three ureolytic bacterial strains from the *Sporosarcina* family, including *S. newyorkensis*, a newly isolated microbe from the deep sea. We find that the interplay between structural water and strain-specific amino acid groups is fundamental to the stabilisation of vaterite and that, under the same conditions, different isolates yield distinctly different polymorphs. The latter is found to be associated with different urease activities and, consequently, precipitation kinetics, which change depending on pressure-temperature conditions. Further, CaCO<sub>3</sub> polymorph selection also depends on the coupled effect of chemical treatment and initial bacterial concentrations. Our findings provide new insights into strain-specific CaCO<sub>3</sub> polymorphic selection and stabilisation, and open up promising avenues for designing bio-reinforced geo-materials that capitalise on the different particle bond mechanical properties offered by different polymorphs.

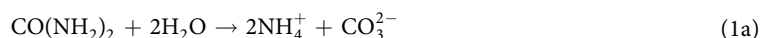
Calcium carbonate (CaCO<sub>3</sub>) makes up almost 4% of the Earth's crust and has been studied extensively due to its importance in biomineralisation in natural environments, including carbon cycling, alkalinity generation, and the biogeochemical cycling of elements<sup>1-3</sup>. In addition to its importance in nature, however, the enhanced mechanical properties of certain biotic calcium carbonates have inspired many studies to try to understand their structural secrets<sup>4-6</sup>, and prompted their use in geotechnical engineering to improve the mechanical response of soils<sup>7-11</sup>. A clear example of these natural materials is nacre in mollusc shells, formed of microlaminated composites of aragonite and/or calcite, each with an associated organic matrix that gives them a fracture toughness 3000 times greater than that of the constituent mineral alone<sup>12</sup>. Clearly, the coupling of a mineral phase with an organic material (*i.e.* biomineral) plays a vital role in the formation and stabilisation of the final CaCO<sub>3</sub> precipitate, in addition to contributing to its ultimate mechanical properties<sup>4,13-17</sup>. However, understanding the interrelationship between biotic precipitation, polymorphism, and long-term stabilisation has proven to be far from trivial.

It is well established that CaCO<sub>3</sub> has three polymorphs: vaterite, aragonite, and calcite, with rhombohedral, orthorhombic and hexagonal structures respectively, in order of decreasing solubility and increasing thermodynamic stability<sup>18</sup>. Additional metastable forms have been noted in the literature, all of which are hydrated: monohydrocalcite (CaCO<sub>3</sub>·H<sub>2</sub>O), ikaite (CaCO<sub>3</sub>·6H<sub>2</sub>O), calcium carbonate hemihydrate (CaCO<sub>3</sub>·1/2H<sub>2</sub>O), and amorphous calcium carbonate (ACC)<sup>19,20</sup>. Thus far, most studies have tackled the formation and crystallisation of CaCO<sub>3</sub> in abiotic systems, with a particular focus on ACC and vaterite as intermediates in the crystallisation of CaCO<sub>3</sub><sup>21-25</sup>. However, in contrast to the unique nature of the equilibrium state, multiple reaction pathways from a given initial condition to that final state of thermodynamic equilibrium may exist. Such reaction pathways can be very sensitive to minor impurities and environmental perturbations, such as the presence of microorganisms, which modify the energy barrier from reactant to product phases<sup>26</sup>. It has even been suggested that organic macromolecules associated with bacterial activity cause the Ostwald step sequence to stop at one of its intermediate stages: ACC → vaterite → calcite<sup>21</sup>, making biotic vaterite precipitation far more common than would

<sup>1</sup>Department of Engineering, University of Cambridge, Cambridge, CB2 1PZ, UK. <sup>2</sup>Department of Engineering, Hiroshima University, Hiroshima, 739-8527, Japan. <sup>3</sup>Department of Engineering, University of California-Berkeley, California, 94720, Berkeley, USA. <sup>4</sup>Department of Earth Sciences, University of Cambridge, CB2 3EQ, Cambridge, UK. <sup>5</sup>Asian School of the Environment, Nanyang Technological University, 50 Nanyang Avenue, 639798, Singapore. ✉e-mail: [ac989@cam.ac.uk](mailto:ac989@cam.ac.uk)

be anticipated in abiotic systems. From a chemical standpoint, the polymorphous composition is governed by the addition of the reactants, which lead to a supersaturation state in which the concentration of calcium and carbonate ions exceed the solubility product of  $\text{CaCO}_3$ <sup>18,27</sup>. This simultaneously triggers the nucleation of crystals and the dissolution of the colloidal ACC precursor<sup>18</sup>. However, local variations of the calcium and carbonate ion activity product (IAP) and thus saturation, can favour the formation of one polymorph over another. Vaterite, for example, typically precipitates in highly supersaturated and moderately alkaline environments<sup>14,21,23</sup>.

Within this context, enzymatic hydrolysis of urea presents a straightforward process to understand the precise role of microbes in microbial induced calcium carbonate precipitation (MICP). This is because the urease enzyme is ubiquitous in microorganisms, yeast, and plants<sup>5,28</sup>. In addition, it can be easily induced using inexpensive chemicals and is the most widely used process in biomediated soil improvement applications. Ureolytic bacteria enzymatically hydrolyse urea ( $\text{CO}(\text{NH}_2)_2$ ), resulting in the production of ammonium ( $\text{NH}_4^+$ ) and dissolved inorganic carbon (DIC), which in turn increase pH and favour  $\text{CaCO}_3$  precipitation in the presence of soluble calcium ions (eq. 1). This study focuses on three different ureolytic bacterial strains, all belonging to the *Sporosarcina* species: *Sporosarcina pasteurii* (ATCC 11859), *Sporosarcina aquimarina* (ATCC BAA-723), and *Sporosarcina newyorkensis*—a newly isolated microbe from the deep sea in offshore Japan extracted by the National Institute of Advanced Industrial Science and Technology (AIST) using pressure-core nondestructive analysis tools<sup>29</sup>. To our knowledge, this has never been studied before. These strains were selected as they proliferate in different isolation environments: surface dry conditions, and shallow and deep sea, respectively.



Our aim is to shed light on the interaction between the components of mineralised biological materials involved in  $\text{CaCO}_3$  precipitation—namely minerals, macromolecules and water—, and understand their influence on the stabilisation of different  $\text{CaCO}_3$  polymorphs. In addition, we wish to understand how strain-specific precipitation kinetics promote and affect this process. For this purpose,  $\text{CaCO}_3$  was precipitated *in vitro* in 14 mL test tubes via the three different ureolytic soil bacteria described above. To ensure analogous reference conditions, strains were cultivated under sterile conditions at the same pressure and temperature—*i.e.*  $P = P_{atm}$  and  $T = 30^\circ\text{C}$ —to an optical density ( $\text{OD}_{600}$ ) of  $\sim 0.5$ , and subsequently subject to identical external treatment conditions. The cementation treatment liquid medium consisted of a premixed solution of an equimolar amount of urea and  $\text{CaCl}_2$  (0.3 M), in addition to  $3\text{gL}^{-1}$  of Nutrient Broth, all dissolved in deionised water. All samples were created using a ratio of bacteria solution to cementation solution of 1:2. Results strongly suggest that the presence of structural water together with specific amino acids is fundamental to the stabilisation of vaterite and that, at the same initial  $\text{OD}_{600}$  and treatment conditions, different strains yield distinctly different polymorphs. For this reason, we compared the precipitation kinetics, and the pressure-temperature dependence of bacterial population and urease activity for the three microorganisms. Finally, *S. pasteurii*—which is the most common soil bacterium used in geotechnical engineering applications—was also investigated under varying urea- $\text{CaCl}_2$  solution concentrations and initial  $\text{OD}_{600}$ . The mineralogy, morphology, and properties of precipitates were characterised using an array of complementary techniques, namely thermogravimetric analysis coupled with mass spectroscopy (TGA-MS), Raman spectroscopy (RM), X-ray powder diffraction (XRD), and scanning electron microscopy (SEM); and the precipitation kinetics of the three microorganisms quantified through measurement of calcium ion ( $\text{Ca}^{2+}$ ) concentrations and pH (Table S4). Ultimately, our results suggest that strain-specific  $\text{CaCO}_3$  precipitation occurs during ureolytic MICP, possibly due to differences in the urease enzyme, and its response to treatment concentrations and pressure-temperature variations, and that  $\text{CaCO}_3$  polymorphism in biotic systems is far more common than previously anticipated. This may have significant implications for biomediated soil improvement systems.

## Results

**Amorphous and crystalline  $\text{CaCO}_3$  polymorphs.** XRD analysis (Fig. 1a) revealed that calcite was the primary polymorph that precipitated in the presence of *S. newyorkensis* (SN01-0.3M), along with small traces of halite resulting from the drying of the marine broth media used to cultivate the isolate<sup>30</sup> (Fig. S1). On the other hand, precipitates of *S. aquimarina* (SA01-0.3M) contained vaterite as a secondary phase to calcite. The XRD spectrum of precipitates of *S. pasteurii* (SP01-0.3M) showed no traces of calcite, but a broad hump in the range of  $15\text{--}40^\circ 2\theta$  consistent with the presence of a poorly-ordered material and matching data reported in the literature for ACC<sup>31,32</sup>.

Thermal analysis of the same samples also showed significant differences (Fig. 1b). *S. newyorkensis* was characterised by the occurrence of three main weight loss steps, at  $217^\circ\text{C}$ ,  $438^\circ\text{C}$ , and  $757^\circ\text{C}$ , corresponding to 2.4, 9.1, and 38.1 wt%, respectively. In contrast, the TGA of precipitates of *S. aquimarina* only showed two main weight loss steps at approximately  $300^\circ\text{C}$  and  $717^\circ\text{C}$ . However, the first derivative (DTG) revealed that the former resulted from the overlap of four peaks at  $184^\circ\text{C}$ ,  $251^\circ\text{C}$ ,  $287^\circ\text{C}$ , and  $348^\circ\text{C}$  (Fig. S2). These values appeared too high to be attributed to physisorbed water—*i.e.* water evaporated below  $115^\circ\text{C}$ <sup>19</sup>—and were thus attributed to weakly ( $\sim 30\text{--}200^\circ\text{C}$ ) and strongly ( $\sim 200\text{--}550^\circ\text{C}$ ) bound water molecules, giving a structural water content of 8.0 wt% from TGA<sup>33</sup>. Furthermore, the large weight loss observed for *S. newyorkensis* and *S. aquimarina* at  $757^\circ\text{C}$  and  $717^\circ\text{C}$  (36.4 wt%), respectively, was consistent with the loss of  $\text{CO}_2$  from the carbonate decomposition, and also provided an independent confirmation that both samples were comprised almost solely of  $\text{CaCO}_3$  phases. Regarding the precipitates of *S. pasteurii*, TGA revealed that below  $250^\circ\text{C}$  there were two distinguishable temperature intervals where weight losses occurred, namely at  $112^\circ\text{C}$  and  $231^\circ\text{C}$ . The total weight loss in these

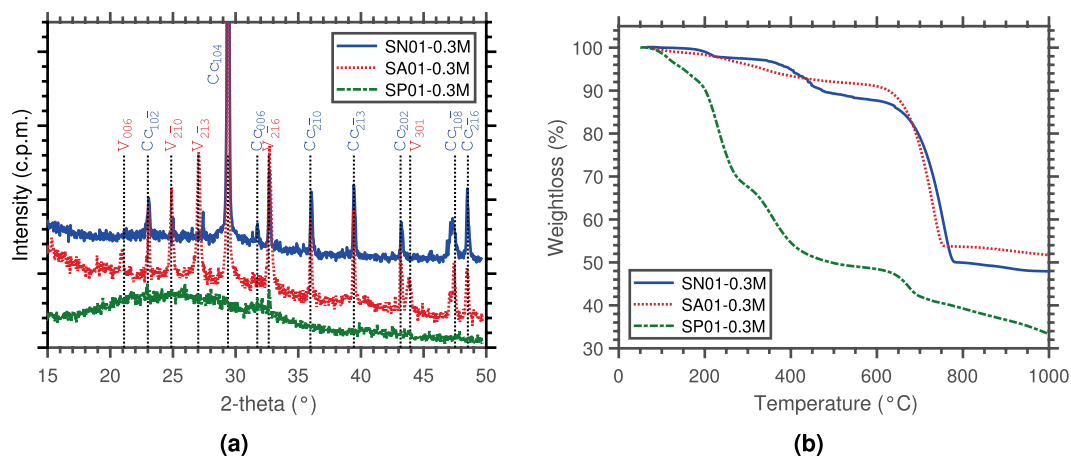


**Figure 1.** XRD pattern with  $hkl$  values of Bragg peaks indicated (Cu-K $\alpha$  radiation,  $\lambda = 1.5406 \text{ \AA}$ ) (a); and TG curves (All: heating rate  $10 \text{ }^\circ\text{C min}^{-1}$ ; SN01-0.3M: Ar “reactive gas” flow rate  $50 \text{ mL min}^{-1}$ , and SA01-0.3M and SP01-0.3M: N $_2$  “reactive gas” flow rate  $50 \text{ mL min}^{-1}$ ) (b) of precipitated CaCO $_3$ , V, vaterite; Cc, calcite; Halite peaks resulting from desiccating media of *S. newyorkensis* not indicated.

transitions was 27 wt% (after physisorbed water removal) and was attributed to dehydration and crystallisation of ACC<sup>34</sup>. The third weight loss was 18 wt% and occurred in the temperature range of 300–550 °C. At such high temperatures, this was unlikely to be caused by the release of structural water, and was thus associated with the pyrolysis of macromolecules, either of organic or inorganic origin. Finally, the thermal peak at 670 °C, matching the decarboxylation of CaCO $_3$ , only accounted for 8 wt% of the weight loss, indicating that minor amounts of CaCO $_3$  were present. The final plateau, slightly inclined, indicated that final weight constancy was not achieved in this sample, possibly due to kinetic effects upon carbonate decomposition<sup>33</sup>.

**Biotic vaterite precipitation.** To further investigate how vaterite and calcite were spatially organised, the precipitates of *S. aquimarina* were examined through Raman spectroscopy. Firstly, spectra were acquired at two visually distinct points of a single crystal. Results are shown in Fig. S3, together with an optical microscopy image of the target collection points. The most prominent features of calcite are the symmetric stretching mode ( $\nu_1$ ) of the carbonate group, followed by two external modes<sup>35,36</sup>. These appeared at 1085 cm $^{-1}$  with a full width at half maximum (FWHM) of 7 cm $^{-1}$ , and at 155 and 280 cm $^{-1}$ , respectively. The identification of other features was not possible due to the high background noise. Raman spectroscopy also helped distinguish vaterite from calcite by comparing the wave numbers of the  $\nu_1$  mode. Indeed, the absorption bands at 1076 and 1088 cm $^{-1}$  corresponding to the symmetric stretching of vaterite<sup>37</sup> were detected in one of the spectra shown in Fig. S3. Secondly, spectra of a single crystal were also collected up to a penetration depth of 25  $\mu\text{m}$ , with results clearly showing a polymorph transition (Fig. 2a). While the characteristic single peak of calcite at 1086 cm $^{-1}$  was detected at the surface, the two peaks at 1076 cm $^{-1}$  and 1088 cm $^{-1}$  appeared within the internal structure. Moreover, the broad nature of the vaterite peak at 1088 cm $^{-1}$  could possibly suggest the combination of two peaks at 1090 and 1085 cm $^{-1}$ , the latter being associated to calcite. This is due to the peak convolution between the polymorphs in this region. In addition, the disappearance of the two lower frequency lattice modes (155 and 280 cm $^{-1}$ ) with penetration depth further supported a transition between carbonate phases. Table S1 lists the peak positions and the corresponding assignments of calcite and vaterite to illustrate the comparison between precipitates of *S. newyorkensis* and *S. aquimarina*.

SEM images of precipitates of *S. aquimarina* showed two distinctive morphologies: (a) spherulites, 5–50  $\mu\text{m}$  in diameter (Fig. S4a), which were associated to vaterite and disphenoid- and dipyrmaid-like calcite crystals (Fig. S4e). Numerous rod-shaped bacterial cells (with length  $\sim 2 \mu\text{m}$  and a diameter of  $\sim 0.5 \mu\text{m}$ ) were observed encased within the growing spherulites, suggesting that the presence of *S. aquimarina* was a prerequisite for their formation. This was further reinforced by the presence of smooth dumbbell CaCO $_3$  morphologies, which have been reported to be uniquely bacterial in origin (Fig. S4b)<sup>38</sup>. In addition, an epoxy cast cross-section of the precipitates (Fig. 2b) revealed hollow cores with walls formed by a fibro-radial internal structure, an observation consistent with spherulite surface features described by<sup>39</sup>. While some cores still showed traces of vaterite spherulites, others had started to be filled by advancing crystallisation steps. Further key aspects of the incorporation of the vaterite spherulites into the calcite crystals were obtained by comparing Fig. S4b–e.

**Indirect evidence for structural amino acids and water.** As evidenced by Fig. S8a–b, the XRD and Raman spectroscopy of precipitates of *S. aquimarina* and *S. newyorkensis* also showed the presence of additional absorption bands that did not correspond to carbonate phases. In particular, the Raman spectra showed the Disorder (D) and Graphite (G) bands typical for organic carbons, with those present in precipitates of *S. newyorkensis* (SN01-0.3M) exhibiting a slightly lower level of organisation than those observed within precipitates of *S. aquimarina* (SA01-0.3M) (see zoomed in plot Fig. S8b and associated supplementary discussion, and Table S2). Consequently, TG-MS analysis on two different powdered samples was used to identify and monitor the evolution of the exhaust gases. MS was set to detect certain  $m/z$  values associated with common fragments from

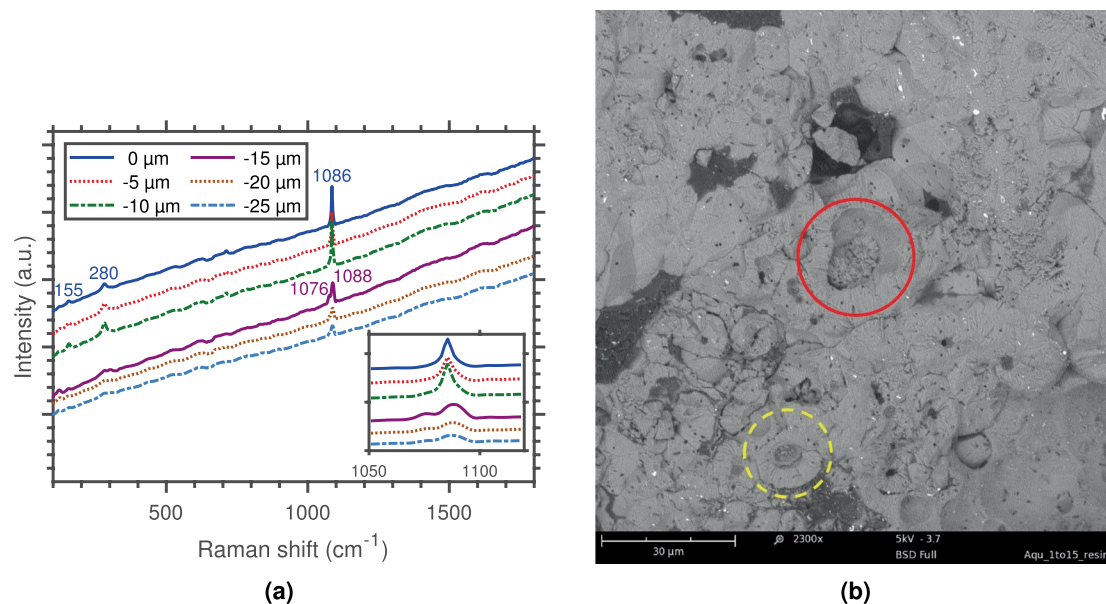


**Figure 2.** Raman spectra of polymorphic  $\text{CaCO}_3$  crystals formed in the presence of *S. aquimarina* (SA01-0.3M) evidencing the coexistence of calcite and vaterite within a single crystal and showing their spatial arrangement (a); and SEM BSE image of internal structure of biotic precipitates of *S. aquimarina* with some cores showing traces of vaterite spherulites (yellow dotted circle) and others that have started to be filled by advancing crystallisation steps (red solid circle) (b).

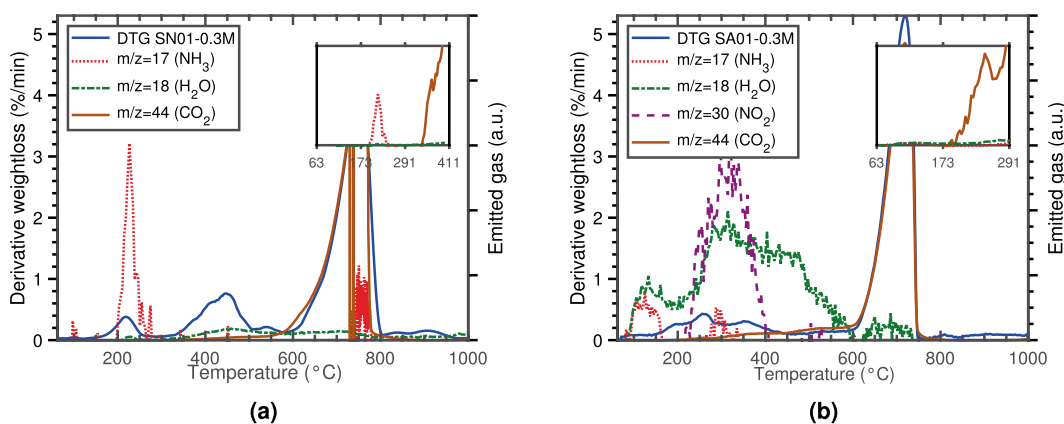


**Figure 3.** DTG and mass spectra of evolved gases measured from coupled TG-MS of  $\text{CaCO}_3$  crystals formed in the presence of: (a) *S. newyorkensis* (heating rate  $10^\circ\text{C min}^{-1}$ ; Ar “reactive gas” flow rate  $50\text{ mL min}^{-1}$ ); and (b) *S. aquimarina* (heating rate  $10^\circ\text{C min}^{-1}$ ;  $\text{N}_2$  “reactive gas” flow rate  $50\text{ mL min}^{-1}$ ).

molecular-ions, listed in Table S3. All MS signals were normalised to a baseline shift value obtained after each experiment from a blank run using an empty crucible. Results therefore refer to relative incremental yields rather than absolute intensity values *per se*. The advantage of this was to be able to compare all exhaust gases using a single plot, allowing for thermal decomposition sequences to be unequivocally identified. The only exception was  $\text{CO}_2$ , plotted on its own intensity axis because its relative yield was considerably higher than that of the other products—understandable given that all of the analysed precipitates were carbonates. Therefore, where discussion warranted, zoomed in plots of the range of temperatures of interest showing the  $\text{CO}_2$  yield with respect to the other products in the group were presented.

The TGA of precipitates of *S. newyorkensis* showed the occurrence of three main weight loss steps. As shown in Fig. 3a,  $\text{CO}_2$  was the main gaseous product in the third step ( $757^\circ\text{C}$ ), associated with the decarbonation of  $\text{CaCO}_3$ . Regarding the first and second steps ( $217$  and  $438^\circ\text{C}$ ), decomposition products mainly included  $\text{NH}_3$  and  $\text{H}_2\text{O}$ , respectively. This indirectly demonstrated the presence of amino acids within the precipitated carbonates and suggested that their primary decomposition included deamination with low yields of dehydration. Using Fourier transform infrared spectroscopy (FTIR), previous studies identified the presence of amino acids within the  $\text{CaCO}_3$  structure of biotic precipitates by the amide I signature at  $1655\text{ cm}^{-1}$ <sup>14,40,41</sup>. Further, FTIR for evolved gas analysis coupled to TGA revealed that the thermal decomposition of organics results in the release of  $\text{CO}$ ,



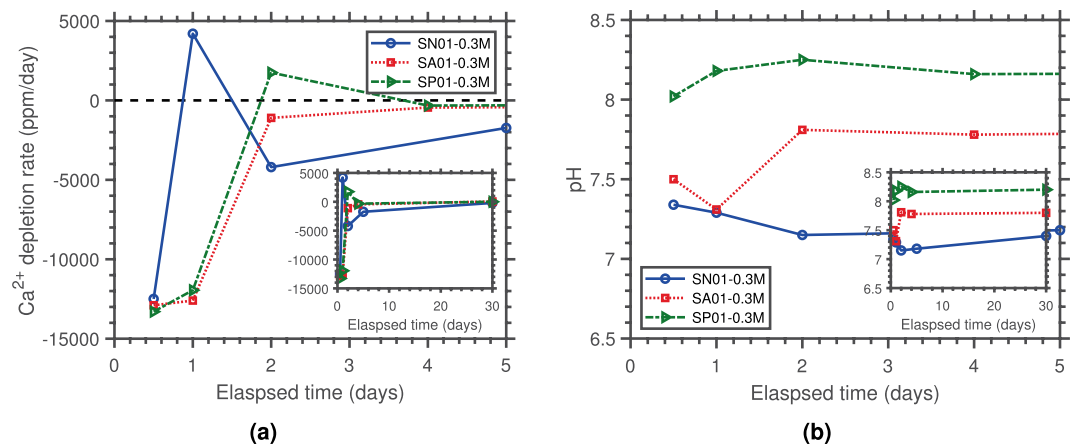


**Figure 4.** Time evolution of the (a) rate of calcium depletion and (b) pH.

CO<sub>2</sub> and NO<sub>2</sub> in the temperature range of 150–500 °C, while amino acids in biotic carbonates also involve the release of NH<sub>3</sub><sup>14</sup>. These results are in agreement with the TG-MS analyses reported here. Moreover, Fig. 3a shows that the rapid releasing rate of NH<sub>3</sub> in the first stage was in sharp contrast with the longer H<sub>2</sub>O and NH<sub>3</sub> releases observed in both the second and third stages respectively, revealing different pathways of formation. In the former, NH<sub>3</sub> was most likely lost as a result of a primary decomposition (*i.e.* individual molecular decomposition of amino acids or formation of an amino radical), while H<sub>2</sub>O in the second stage may have been produced following secondary reactions<sup>42,43</sup>. One interesting observation was that CO<sub>2</sub> was not released during the first stage (see zoomed in plot of Fig. 3a), suggesting that less common aromatic β-amino acids were present<sup>42</sup> (Fig. S8b).

Regarding precipitates of *S. aquimarinus*, their pyrolysis was markedly different (Fig. 3b), with the first two decompositions being less sharp and partially overlapping. The most conspicuous feature was that water remained a structural constituent up to 600 °C, gradually being released from 100 °C (8 wt%). Additionally, the fragmentation products and sequence of precipitates indirectly suggested different starting amino acids, with deamination being a primary, although minor, mode of decomposition. This was echoed by the small NH<sub>3</sub> peak measured between 100–160 °C, previously observed during the pyrolysis of α-amino acids and attributed to the existence of an intermediate<sup>44</sup>. On the other hand, a second process, also considered to be a primary decomposition mode, was the decarboxylation reaction of α-amino acids to produce CO<sub>2</sub> and amines<sup>42,44</sup>. This was evidenced by the CO<sub>2</sub> peak measured at 243 °C (see zoomed in plot of Fig. 3b). Following this primary decomposition, a number of secondary products arise, possibly from the fragmentation of the amines themselves (see supplementary discussion for further details on the pyrolysis of amino acids).

**CaCO<sub>3</sub> precipitation kinetics.** With approximately equal OD<sub>600</sub> ~ 0.5 but different (specific) urease activities (Table S4), it is suggested that the mineralogy, morphology and properties of the precipitated CaCO<sub>3</sub> can be controlled by ureolytic strains with different urease activities and, consequently, precipitation kinetics—quantified through measurement of calcium ion (Ca<sup>2+</sup>) concentrations and pH<sup>45</sup>.

Equal concentrations of Ca<sup>2+</sup> ions and bacterial densities were initially present in all tests, with CO<sub>3</sub><sup>2-</sup> ion concentrations being equal to zero until the onset of urea hydrolysis. As a result, initial calcium depletion rate—calculated as the change in Ca<sup>2+</sup> ion concentration over a certain period of time,  $dCa^{2+}/dt$ —was most closely associated with the nucleation of CaCO<sub>3</sub> for each microorganism<sup>45</sup>. A lower initial urease activity was associated with a faster initial calcium depletion rate from solution (*cf.* Table S4 and Fig. 4a). Comparing the results for *S. pasteurii* (SP01-0.3M) with those for *S. newyorkensis* (SN01-0.3M) and *S. aquimarinus* (SA01-0.3M) it is clear that *S. pasteurii*'s metabolic activity was able to initially hydrolyse more urea into CO<sub>3</sub><sup>2-</sup> ions in the same period of time. This resulted in alkalinity generation and ammonia release, which respectively caused a rapid increase in supersaturation and pH. This provided the high crystallisation kinetics needed for the spherulitic precipitation of ACC, which proceeds via a fast nucleation-controlled mechanism<sup>46</sup>—again evidenced by the higher initial calcium depletion rate. Further, the ACC-vaterite transformation in precipitates of *S. aquimarinus* manifested by a slow decrease in pH associated with the release of water molecules during dissolution; and by a decreasing Ca<sup>2+</sup> depletion rate associated with the release of Ca<sup>2+</sup> ions stored in ACC and their re-precipitation into vaterite. Conversely, this dissolution (and associated pH drop) was not observed in SP01-0.3M, further reinforcing the stabilisation of ACC.

The initial Ca<sup>2+</sup> depletion rate was smallest for *S. newyorkensis*, indicating a slower nucleation event. Interestingly, this reversed as Ca<sup>2+</sup> ions returned to solution, suggesting the early dissolution of Ca-containing precipitates (most likely ACC). As with the initial calcium depletion rate, the timing of this transition appeared to depend on the microorganism. For *S. newyorkensis*, with the highest urease activity, this transition occurred earlier than for the other two less ureolytic microorganisms. Figure 4b further suggests that this process was highly pH-dependant. For *S. newyorkensis* (pH ≈ 7–7.5), calcium ions returned to solution within the first 24 h, and depleted again following a second nucleation event (calcite). This reinforced a direct ACC-calcite transformation when initial pH values are closer to neutral suggested in the literature<sup>46</sup>. With increased pH however, vaterite

(pH  $\approx$  7.5–7.8) and ACC (pH  $\approx$  7.8–8.3) were stabilised by *S. aquimarina* and *S. pasteurii*, respectively. This was linked to a delayed return of  $\text{Ca}^{2+}$  to solution.

An additional consideration is that the pressure-temperature conditions in the environments where the three bacterial strains proliferate are substantially different, thus affecting bacterial growth and urease activity. These parameters were therefore investigated during a 4-day cultivation at two different pressures (1 atm, 3 MPa) and three different temperatures (4 °C, 15 °C, 30 °C). Interestingly, results showed that the effect of temperature on  $\text{OD}_{600}$  was more pronounced than that of pressure (Figs. S5a and S6a), and that (specific) urease activity was most sensitive to pressure at temperatures near those of the original isolation environment (Fig. S5b,c). Fig. S6b shows that a loss of specific urease activity with pressure for all three ureolytic microorganisms, suggesting that pressure potentiates inhibitory factors that affect the function of the urease enzyme. It is also clear that aside from pressure and temperature, time played an important role, with the following conditions yielding a maximum specific urease activity (all at  $P = 1$  atm): *S. newyorkensis*, 1-day cultivation,  $T = 4$  °C; *S. aquimarina*, 1-day cultivation,  $T = 15$  °C; and *S. pasteurii*: 4-day cultivation,  $T = 30$  °C.

**Cooperative effect of bacterial and treatment concentrations.** We further extended our study by investigating the influence of  $\text{OD}_{600}$  and urea- $\text{CaCl}_2$  solution molarity on polymorphic selection for *S. pasteurii* (Fig. S7). For example, SP02-0.02M-D refers to *S. pasteurii* treated with 0.02 Molar of  $\text{CaCl}_2$  and with a diluted  $\text{OD}_{600}$  of 1.38. TGA showed that samples treated with 0.02 and 0.2 M displayed almost identical thermogram profiles between bacterial concentrations (Fig. S7a–d). Close examination of the 0.02 M samples (D and ND) disclosed that in both cases the amount of  $\text{CaCO}_3$  was  $\sim 15$ –30 wt%, which was found to be in agreement with values reported in other biotic studies of ACC<sup>15,47</sup>. Furthermore, two distinguishable temperature intervals where weight loss occurred were measured below 250 °C. These were accompanied by broad peaks at around 110 and 230 °C and were attributed to the release of water molecules. This double dehydration behaviour was also consistent with previous studies<sup>15,47,48</sup>. The total weight loss in this transition was 15–16 wt%, which was compatible with a stoichiometry of  $\text{CaCO}_3 \cdot \text{H}_2\text{O}$ . Finally, a third weight loss region of approximately 25 wt% occurred in the temperature range of 250–500 °C. At such high temperatures, this loss could be attributed to either strongly bound water molecules and/or to the secondary decomposition of amines (cf. Fig. 3a). The wider nature of this peak (i.e. slower release), however, lent some support to the existence of secondary reactions (see supplementary discussion on the pyrolysis of ACC and Fig. S12). Acquisition of XRD patterns for the 0.02 M samples was not possible due to the low volume of precipitates available. However, the similarities between the thermal decomposition observations made for these samples and SP01-0.3M, allowed us to conclude that XRD patterns would have been very similar to the one showed in Fig. 1a and attributed to ACC.

The TGA of precipitates resulting from the 0.2 M solutions (both D and ND) showed a clear peak at around 760 °C ( $\sim 40$  wt%), corresponding to the decomposition of  $\text{CaCO}_3$ . In addition, their TG profiles were very similar to the profile obtained for precipitates of *S. aquimarina* (cf. Fig. 1b), with two small peaks at approximately 220 °C and 320 °C (8.2 wt%). Taken together, these results corroborated the presence of water within the crystal structure with a stoichiometry of  $\text{CaCO}_3 \cdot 1/2\text{H}_2\text{O}$ <sup>19</sup>. In addition, the XRD measurements showed the presence of both vaterite and calcite, but no extra reflections attributed to crystalline hydrated phases were apparent (Fig. S7e,f).

Bacterial concentration had a greater effect at a solution concentration of 1 M, with calcite being the only phase detected at high  $\text{OD}_{600}$  (SP03-1M-ND Fig. S7f) and vaterite at low  $\text{OD}_{600}$  (SP02-1M-D Fig. S7e). The TGA of these samples provided further valuable insights into their properties. While SP03-1M-ND (Fig. S7b,d) showed a sharp peak at 240 °C—matching the first peak observed for *S. newyorkensis* (cf. Fig. 3a) and associated to the pyrolysis of amino acids—, the thermal decomposition of SP01-1M-D (Fig. S7a,c) started at a lower temperature (220 °C) and was accompanied by a second peak at 327 °C. In consistency with previous observations made for precipitates containing vaterite, and by comparing this profile with the MS results for precipitates of *S. aquimarina* (cf. Fig. 3b), results strongly suggested the presence of structural water and amino acids. Finally, both samples displayed a significant weight loss at 740 °C, corresponding to the decarbonation of  $\text{CaCO}_3$ .

## Discussion

*S. aquimarina* induced the formation of highly porous rounded polycrystals, which had no well defined structure. Raman spectra collected for a single crystal up to a penetration depth of 25  $\mu\text{m}$  showed a transition from calcite to vaterite with depth, evidenced by the splitting of the  $\nu_1$  mode into two peaks (Fig. 2a). To our knowledge, such Raman characterisation of  $\text{CaCO}_3$  polymorphs has never before been carried out and provides further evidence that biotic calcite initiates from a metastable phase rather than from a crystalline nucleus leading to single crystals. Moreover, hollow cores with walls formed by a concentric channel-like structure of interconnected pores were observed by SEM and suggested radial growth<sup>49</sup>. While some cores still showed traces of vaterite spherulites, others had already started to be filled by advancing crystallisation steps (Fig. 2b). This morphology further reinforced the existence of a metastable precursor, which adopts a spherical structure to minimise its surface contact with the surroundings<sup>15</sup>, and provided significant evidence of a vaterite-calcite transformation.

Furthermore, our results indirectly showed that vaterite only stabilised when water molecules and amino acids were present in the crystal structure—i.e. SA01-0.3M, and SP02-0.2M-D and SP03-0.2M-ND. The idea that organic macromolecules can stabilise vaterite has been suggested previously, both in biotic<sup>14</sup> and abiotic<sup>50,51</sup> systems. However, their presence alone as a justification for stabilisation seems unlikely as precipitates of *S. newyorkensis* only showed calcite peaks despite containing amino acids within their structure (Fig. 1a and Fig. S1). According to our TGA data, precipitates containing vaterite also comprised of half a molecule of water per one molecule of  $\text{CaCO}_3$ . Therefore, global rationalisation of these results was possible by considering water molecules, potentially from small amounts of additional hydrated phases that become structurally interrelated with the crystal structure. This likely happens via a hydrogen bond between the amino acid surface along the edge of the crystal and the water molecule. This scenario was supported by the different composition of amino acids in

precipitates of *S. newyorkensis* and *S. aquimarina* (see supplementary discussion on pyrolysis of amino acids). Hence, our results, as well as those of other studies<sup>52,53</sup>, suggest that only specific amino acid groups interact with the CaCO<sub>3</sub> surface, thus having an effect on the properties of the precipitated phases. In particular, polar hydrophilic amino acids—*i.e.* those amino acids that have oxygen and nitrogen atoms and with an unequal distribution of electrons—would be the only ones able to form hydrogen bonds with water molecules, either as proton donors or acceptors. The presence of nitrogen during the pyrolysis of precipitates of *S. aquimarina* lent some support to the existence of these hydrophilic amino acids within the crystal structure.

To better understand the underlying mechanisms during strain-specific ureolytic precipitation of CaCO<sub>3</sub>, the precipitation kinetics were quantified and compared. Results showed that the precipitation (or not) of ACC or vaterite as precursors and/or intermediates of calcite could be favoured by selecting microorganisms with appropriate urease activities, and therefore, precipitation kinetics (*cf.* Fig. 4 and Table S4). *S. pasteurii*, the low-urease activity microorganism, had the fastest initial nucleation kinetics, and *S. newyorkensis*, the high-urease activity microorganism, had the slowest initial nucleation kinetics. Subsequently, crystallisation pathways of CaCO<sub>3</sub> polymorphs appeared to be highly pH- and dissolution rate-dependant. High pH and longer dissolution times following a fast nucleation event prompted ACC stabilisation (SP01-0.3M); while a pH closer to neutral and shorter dissolution times following a slower nucleation event promoted an ACC-calcite transformation (SN01-0.3M). Values for *S. aquimarina* (SA01-0.3M), yielding an ACC-vaterite-calcite transformation, were in between. Moreover, regardless of the formation pathway, CaCO<sub>3</sub> polymorph transformation involved the release of water (and the associated pH drop). Therefore, these results provide additional evidence that controlling dissolution kinetics is essential to controlling polymorph stabilisation. Nonetheless, establishing the specific mechanism via which this occurs requires direct amino acid analysis.

Because the kinetics of mineralisation were found to depend on (specific) urease activity, we sought to understand the role of cultivation conditions. Findings suggest that OD<sub>600</sub> is most sensitive to temperature, whilst (specific) urease activity displayed a more complex pressure-temperature dependence. The increase in OD<sub>600</sub> with temperature (Fig. S5a), most notable for *S. newyorkensis* and *S. aquimarina*, may, to some extent, be attributed to the decrease in dissolved oxygen contents. Indeed, an oxygen-limited environment would have prompted the growth of (facultative) anaerobic microorganisms. There is however a large body of research supporting the idea that pressure and temperature do not only affect the microbial ecology of aqueous environments, but also the structural stability of biomolecules<sup>54–56</sup>, the cell membrane composition<sup>57</sup>, and the physiology of bacterial cells<sup>58</sup>. Therefore, further work is required to assess the role of pressure and temperature on these processes, as well as on how they affect the preferred CaCO<sub>3</sub> phase precipitated by the bacterial strains studied here.

Results showed that optimum conditions for CaCO<sub>3</sub> polymorphism are both strain- and environment-dependant (*i.e.* urea-CaCl<sub>2</sub> solution, pressure, temperature). Under the same bacterial concentrations and environmental conditions the three bacterial strains studied herein produced different polymorphs (Fig. 1a), most likely due to the differences in their urea hydrolysis metabolism process. In addition, the results for *S. pasteurii* showed a coupling between the concentration of ions in solution (*i.e.* supersaturation) and the initial bacterial concentrations. Results suggested that the higher the ionic strength, the stronger the interaction between background ions and water becomes. This reduced the availability of water molecules in the solution, favouring clustering and dehydration, and thus precipitation. Conversely, at low ionic strengths, dehydration was hindered due to the higher availability of water molecules in the solution<sup>6</sup>. This promoted hydrophilic interactions between amino acid and water molecules, affecting the dissolution-reprecipitation via which vaterite transforms into calcite. It is worth pointing out that in biotic systems, high ionic strength is attained through the combination of high bacterial concentrations—*i.e.* yielding high carbonate ion concentrations—and high urea-CaCl<sub>2</sub> solution concentrations, and it is this trade-off between the two that will determine whether metastable polymorphs stabilise or not.

## Implications for geotechnical engineering

As a general rule, calcite has been the only CaCO<sub>3</sub> polymorph reported for geotechnical engineering applications, as this is thought to be less prone to alteration, *i.e.* more stable. However, this study supported the notion that ACC and vaterite are much more abundant in CaCO<sub>3</sub> biomineralisation than previously believed, and clarifying how they are formed and stabilised may have broader implications for the mechanical properties of cemented sands. Generally speaking, the role of MICP in sands is to create an adhesive bond at the inter-particle contacts, enhancing their load-carrying capacity. In this context, particle contact properties will both be affected by the degree of cementation and the nature of the cementing bond (*e.g.* morphology, mineralogy, properties). Both numerical and experimental data have shown that increasing the cementation level enhances the maximum shear strength and stiffness at small strains, and as the cementation increases the stress-strain behaviour transitions from ductile to brittle<sup>9,59,60</sup>. From an engineering standpoint, this leads to an unwanted soil response because brittle materials absorb little plastic energy prior to fracture, and thus fail catastrophically. Clearly, it is also noted that different CaCO<sub>3</sub> polymorphs yield different particle contact properties, leading to variations in their strengthening effect. DEM analyses in the literature have shown that an increase in inter-particle friction brings the stress-strain response of granular materials from ductile to brittle, and augments the anisotropic distribution of contact forces<sup>61</sup>. For the specific case of MICP-treated soils, studies further concluded that increasing calcite content results in a few heavily loaded particle contacts transmitting a large proportion of the load, thus making the force distributions become increasingly non-uniform<sup>59</sup>. This is consistent with the fact that higher friction values tend to decrease the mean contact number per particle<sup>61</sup>.

Of key importance therefore, is that the CaCO<sub>3</sub> polymorph selection may be controlled through selection of a bacterial strain with appropriate precipitation kinetics, while metastable polymorph stabilisation may be controlled by inhibiting dissolution through the interplay between specific amino acid groups and water within the crystal structure. Further, this study showed that ureolytic microorganisms common to geotechnical engineering

environments not only adapt to the urea-CaCl<sub>2</sub> solution by modulating the precipitation kinetics, but that this interaction is very sensitive to pressure and temperature. In particular, the increased sensitivity of urease activity to pressure at temperatures near those of the original isolation environment is of major importance for the application of MICP in the deep sea, where both high pressure and low temperature combine to produce a highly hostile environment for bacterial viability.

Results for *S. pasteurii* further revealed that biotic precipitation of calcite alone required both high urea-CaCl<sub>2</sub> solution concentrations and high bacterial concentrations, treatment conditions that would yield substantial amounts of ammonium ions (NH<sub>4</sub><sup>+</sup>), a hazardous byproduct of urea hydrolysis. However, using a bacterial strain that is able to produce the desired polymorph at lower bacterial and treatment concentrations (e.g. *S. newyorkensis*) offers potential to lower the yield of this byproduct. Therefore, an optimisation exercise between bacterial and treatment concentrations is required on a strain-specific basis for biotechnological applications.

## Methods

**Bacterial strains and cultivation.** Three different ureolytic CaCO<sub>3</sub>-precipitating species were used in the present study: *Sporosarcina pasteurii* (ATCC 11859), *Sporosarcina aquimarina* (ATCC BAA-723), and *Sporosarcina newyorkensis*—a newly isolated microbe from the deep sea in offshore Japan. They were selected because they proliferate in different isolation environments: surface dry conditions, and shallow and deep sea, respectively. Thus, we emphasise that results presented herein did not necessarily represent a unique group of CaCO<sub>3</sub>-precipitating bacteria, but rather, organisms that proliferate and express the urease gene under the cultivation conditions used.

Both *S. pasteurii* and *S. aquimarina* were cultivated under sterile conditions in ATCC 1376 NH<sub>4</sub>-YE medium in a shaking incubator (approximately 24 h at 30 °C and 200 rpm). Bacterial colonies were stored in MB agar plates in a refrigerator at 4 °C for up to one month before resuspending them in a fresh medium by the aforementioned process. Regarding *S. newyorkensis*, this was cultivated from a freeze-dried stock and resuspended under sterile conditions in ATCC 2216 Marine Broth medium in a shaking incubator (approximately 24 h at 30 °C and 200 rpm). Similarly, this strain was stored in MB agar plates in a refrigerator at 4 °C for up to one month. All three strains were harvested at an optical density of ~0.5, measured at a wavelength of 600 nm (OD<sub>600</sub>). In addition, *S. pasteurii*—which is the most common soil bacterium used in geotechnical engineering applications—was also investigated under varying urea-CaCl<sub>2</sub> solution concentrations and initial bacterial densities (OD<sub>600</sub>).

To ensure analogous reference conditions, all bacterial strains were cultivated under the same pressure and temperature—i.e.  $P = P_{atm}$  and  $T = 30$  °C. It is acknowledged however that the environments from which the isolates were obtained could also have a selective influence on their viability. In this regard, the three bacterial strains were cultivated in static conditions during a 4-day period at varying temperatures—i.e. 4 °C, 15 °C, and 30 °C—, and pressures—i.e. 1 atm and 3 MPa—, and the bacterial density and urease activity were assessed.

**Cementation solution.** The cementation solution for MICP treatment was created using calcium chloride (CaCl<sub>2</sub>), urea (CO(NH<sub>2</sub>)<sub>2</sub>) and Thermo Scientific Oxoid Nutrient Broth dissolved in deionised (DI) water. It was not autoclaved. CaCO<sub>3</sub> was precipitated *in vitro* in 14 mL test tubes at room temperature (each with a bacteria to cementation solution ratio of 1:2) and via the three different ureolytic soil bacteria described above. Precipitates were preserved after more than 30 days in the mother culture medium. Before further analysis, the solution was decanted, and solids collected and dried in an oven at 100 °C for 24 h to remove adsorbed water. Table S4 summarises the MICP treatment formulations and characterisation techniques used in the present study.

**Biochemistry.** *Bacterial density.* A Thermo Scientific Helios Zeta spectrophotometer was used to measure bacterial cell concentration—i.e. optical density—at a wavelength of 600 nm (OD<sub>600</sub>). The degree of turbidity of the bacterial medium was directly related to the number of microorganisms present, both viable and dead cells. A higher turbidity therefore indicated a higher microbial cell mass. For the used apparatus, photometric accuracy decreased for OD<sub>600</sub> > 2.0; in this case, the solution was diluted using a blank NH<sub>4</sub>-YE or MB broth medium, and the obtained OD<sub>600</sub> multiplied by the dilution factor.

*Urease activity.* The hydrolysis reaction of urea (eq. 1a) generates an increase in the overall electrical conductivity of the solution, linearly proportional to the concentration of active urease (eq. 2a). Urease activities of bacterial cells were thus determined by measuring the relative change in electrical conductivity when the bacterial solution was exposed to 1.11 M urea for a 5 min-duration. Subsequently, the rate of conductivity increase was converted to urea hydrolysis rate using eq. 2b. Finally, specific urease activity, defined as the urease activity by unit biomass, was calculated according to the following eq. 2c<sup>28</sup>.

$$\text{Urea hydrolysed (mM)} = \text{Conductivity (mS cm}^{-1}\text{)} \times 11.11 \quad (2a)$$

$$\text{Urea seactivity (mM h}^{-1}\text{)} = \frac{\Delta \text{Conductivity } (\mu\text{S cm}^{-1})}{\Delta t \text{ (min)}} \times \frac{10^{-3} \text{ mS}}{1 \mu\text{S}} \times \frac{60 \text{ min}}{1 \text{ h}} \times 11 \cdot 11 \quad (2b)$$

$$\text{Specific urea seactivity (mM h}^{-1}\text{OD}_{600}^{-1}\text{)} = \frac{\text{Urea seactivity (mM h}^{-1}\text{)}}{\text{Biomass (OD}_{600}\text{)}} \quad (2c)$$

*pH:* pH was measured with a LAQUAtwin Compact pH Meter B-71X (range, 2.0–12.0 pH, ±0.1).



**Aqueous calcium:** Aqueous calcium was measured with a LAQUAtwin Compact Ca<sup>2+</sup> Meter B-751 (range, 4–9900 mgL<sup>-1</sup>).

**Characterisation.** *Raman spectroscopy (RM).* A confocal Horiba Jobin Yvon LabRAM 300 Raman spectrometer of 300 mm focal length at the Department of Earth Sciences, University of Cambridge was used to collect Raman spectra in the 100–1800 cm<sup>-1</sup> spectral range. A holographic grating of 1800 gr mm<sup>-1</sup> coupled to a Peltier front illuminated CCD detector (1024 × 256 pixel in size) enabled a spectral resolution of ~1 cm<sup>-1</sup>. The excitation line at 532.05 nm was produced by a Laser Quantum Ventus 532 laser source focused on the sample using an Olympus LMPLFLN 50× long working distance objective. Collected Raman spectra were treated by PeakFit software (v4 for Win32)<sup>62</sup>. For each spectrum, the baseline was subtracted and peak features were determined by least squares fitting to Voigt profiles for the Raman bands. Peak positions were calibrated against the measured excitation of a Ne light reference spectrum<sup>63</sup>.

*X-Ray Powder Diffraction (XRD).* Measurements were performed at the Department of Earth Sciences, University of Cambridge using a Theta-theta Bruker D8 equipped with a copper sealed tube x-ray source producing Cu-K α radiation at a wavelength of 1.5406 Å from a generator operating at 40 keV and 40 mA. Scanning rate was 0.03° 2θ per minute from 15 to 50°. In addition, samples suspected to contain hydrated crystal phases (SA01-0.3M, SP02-0.2M-D, and SP03-0.2M-ND) were also analysed from 3 to 50°. Only a broad hump in the range 4–9° 2θ was consistently detected. Immediately after the acquisition a blank pattern was also acquired to exclude the possibility of noise from the sample holder. Diffractograms were interpreted using DIFFRAC.EVA software (v4.3.1)<sup>64</sup>.

*Thermal analysis (TGA).* Experiments were performed using a Mettler Toledo TGA/DSC 1 Star<sup>e</sup> System analyser with a horizontal reaction chamber (Department of Engineering, University of Cambridge). Around 10–30 mg of sample were placed in a cylindrical 70 μL alumina crucible (ID 4.9 mm, depth 4 mm). The TGA furnace was constantly purged with 100 mL of Ar gas. Samples were heated from 50 °C to 1000 °C at a heating rate of 10 C°/min in a stream of N<sub>2</sub> or Ar “reactive gas” provided directly above the sample with a flow rate of 50 mL min<sup>-1</sup>. A baseline, obtained under the same conditions with an empty alumina crucible, was subtracted from the measured thermograms.

*Mass spectroscopy (MS).* The out-gas from TGA was directed to a quadrupole mass spectrometer, Hiden Analytical, HAL IV RC (Department of Engineering, University of Cambridge), to detect the presence of NH<sub>3</sub> (m/z = 17), H<sub>2</sub>O (m/z = 18), CO (m/z = 28), NO<sub>2</sub> (m/z = 30), and CO<sub>2</sub> (m/z = 44). The measurements were performed using an SEM detector. The gas components were fragmented at 70 eV. To analyse a possible drift in time, a blank run obtained with an empty alumina crucible was performed after each experiment. The signal at m/z = 17 can be contributed both to NH<sub>3</sub> and to [OH<sup>+</sup>], a fragment ion of water. The contribution of the [OH<sup>-</sup>] ion was evaluate as 20% of the m/z = 18 signal value, and extracted from the signal at m/z = 17. The remaining signal at m/z = 17 was assigned to ammonia. All MS signals were normalised to a baseline shift value obtained after each experiment from a blank run using an empty crucible. Results therefore refer to relative incremental yields rather than absolute intensity values *per se*. The advantage of this was to be able to compare all exhaust gases using a single plot, allowing for thermal decomposition sequences to be unequivocally identified. The only exception was CO<sub>2</sub>, plotted on its own intensity axis because its relative yield was considerably higher than that of the other products—understandable given that all of the analysed precipitates were carbonates. Therefore, where discussion warranted, zoomed in plots of the range of temperatures of interest showing the CO<sub>2</sub> yield with respect to the other products in the group were presented.

*Scanning electron microscopy (SEM).* Images of precipitates were obtained using a Phenom Pro Generation 5 (Department of Engineering, University of Cambridge). To observe the internal structure, epoxy casts of precipitates were made through the epoxy vacuum cast-embedding technique. Each mould was then cut to expose a fresh surface and polished using progressively finer grades of silicon carbide (SiC) paper (Grit 180–4000) and polishing alumina (1 and 0.3 μm). To observe the morphology, precipitates were dispersed onto a carbon adhesive-coated aluminium SEM mount and settled with a short burst of air. All samples were uncoated and images were acquired under backscattered scanning electron microscopy mode (SEM BSE) at a maximum resolution of 2048 × 2176 pixels.

Received: 31 December 2019; Accepted: 21 May 2020;

Published online: 23 June 2020

## References

1. Stocks-Fischer, S., Galinat, J. K. & Bang, S. S. Microbiological precipitation of CaCO<sub>3</sub>. *Soil Biol. Biochem.* **31**, 1563–1571, [https://doi.org/10.1016/S0038-0717\(99\)00082-6](https://doi.org/10.1016/S0038-0717(99)00082-6) (1999).
2. Mitchell, A. C. & Ferris, F. G. The Influence of *Bacillus pasteurii* on the Nucleation and Growth of Calcium Carbonate. *Geomicrobiol. J.* **23**, 213–226, <https://doi.org/10.1080/01490450600724233> (2006).
3. Warren, L. A., Mauri, P. A., Parmar, N. & Ferris, F. G. Microbially Mediated Calcium Carbonate Precipitation: Implications for Interpreting Calcite Precipitation and for Solid-Phase Capture of Inorganic Contaminants. *Geomicrobiol. J.* **18**, 93–115, <https://doi.org/10.1080/01490450151079833> (2001).
4. Weiner, S. & Addadi, L. Design strategies in mineralized biological materials. *J. Mater. Chem.* **7**, 689–702, <https://doi.org/10.1039/A604512J> (1997).
5. Hammes, F., Boon, N., de Villiers, J., Verstraete, W. & Siciliano, S. D. Strain-Specific Ureolytic Microbial Calcium Carbonate Precipitation. *Appl. Environ. Microbiol.* **69**, 4901–4909, <https://doi.org/10.1128/AEM.69.8.4901-4909.2003> (2003).

6. Burgos-Cara, A., Putnis, V., Rodriguez-Navarro, C. & Ruiz-Agudo, C. E. Hydration Effects on the Stability of Calcium Carbonate Pre-Nucleation Species. *Minerals* **7**, 126, <https://doi.org/10.3390/min7070126> (2017).
7. Van Paassen, L. A. Biogrout (ground improvement by microbially induced carbonate precipitation). Ph.D. thesis, Delft University of Technology (2009).
8. Al Qabany, A. & Soga, K. Effect of chemical treatment used in MICP on engineering properties of cemented soils. *G@ACUTEACCENT@eotechnique* **63**, 331–339, <https://doi.org/10.1680/geot.SIP13.P022> (2013).
9. Montoya, B. & Dejong, J. Stress-Strain Behavior of Sands Cemented by Microbially Induced Calcite Precipitation. *J. Geotech. Geoenvironmental Eng.* **141**, 4015019, [https://doi.org/10.1061/\(ASCE\)GT.1943-5606.0001302](https://doi.org/10.1061/(ASCE)GT.1943-5606.0001302) (2015).
10. Terzis, D., Bernier-Latmani, R. & Laloui, L. Fabric characteristics and mechanical response of bio-improved sand to various treatment conditions. *Géotechnique Lett* **6**, 50–57, <https://doi.org/10.1680/jgele.15.00134> (2016).
11. Jiang, N.-J. & Soga, K. The applicability of microbially induced calcite precipitation (MICP) for internal erosion control in gravel-sand mixtures. *G@ACUTEACCENT@eotechnique* **67**, 42–55, <https://doi.org/10.1680/jgeot.15.P182> (2017).
12. Falini, G. Crystallization of calcium carbonates in biologically inspired collagenous matrices. *Int. J. Inorg. Mater.* **2**, 455–461, [https://doi.org/10.1016/S1466-6049\(00\)00040-4](https://doi.org/10.1016/S1466-6049(00)00040-4) (2000).
13. Falini, G., Albeck, S., Weiner, S. & Addadi, L. Control of Aragonite or Calcite Polymorphism by Mollusk Shell Macromolecules. *Science* **271**, 67–69, <https://doi.org/10.1126/science.271.5245.67> (1996).
14. Rodriguez-Navarro, C., Jimenez-Lopez, C., Rodriguez-Navarro, A., Gonzalez-Muñoz, M. T. & Rodriguez-Gallego, M. Bacterially mediated mineralization of vaterite. *Geochimica et Cosmochimica Acta* **71**, 1197–1213, <https://doi.org/10.1016/j.gca.2006.11.031> (2007).
15. Raz, S., Testeniere, O., Hecker, A., Weiner, S. & Luquet, G. Stable Amorphous Calcium Carbonate Is the Main Component of the Calcium Storage Structures of the Crustacean *Orchestia cavimana*. *The Biol. bulletin* **203**, 269–274, <https://doi.org/10.2307/1543569> (2003).
16. Kim, Y.-Y. *et al.* An artificial biomineral formed by incorporation of copolymer micelles in calcite crystals. *Nat. Mater.* **10**, 890 (2011).
17. Rae Cho, K. *et al.* Direct observation of mineral–organic composite formation reveals occlusion mechanism. *Nat. Commun.* **7**, 10187 (2016).
18. Kitamura, M. Crystallization and Transformation Mechanism of Calcium Carbonate Polymorphs and the Effect of Magnesium Ion. *J. Colloid Interface Sci.* **236**, 318–327, <https://doi.org/10.1006/jcis.2000.7398> (2001).
19. Zou, Z. *et al.* A hydrated crystalline calcium carbonate phase: Calcium carbonate hemihydrate. *Science* **363**, 396–400, <https://doi.org/10.1126/science.aav0210> (2019).
20. Thili, M. *et al.* Characterization of CaCO<sub>3</sub> hydrates by micro-Raman spectroscopy. *J. Raman Spectrosc.* **33**, 10–16, <https://doi.org/10.1002/jrs.806> (2002).
21. Ogino, T., Suzuki, T. & Sawada, K. The formation and transformation mechanism of calcium carbonate in water. *Geochimica et Cosmochimica Acta* **51**, 2757–2767, [https://doi.org/10.1016/0016-7037\(87\)90155-4](https://doi.org/10.1016/0016-7037(87)90155-4) (1987).
22. Sheng Han, Y., Hadiko, G., Fuji, M. & Takahashi, M. Crystallization and transformation of vaterite at controlled pH. *J. Cryst. Growth* **289**, 269–274, <https://doi.org/10.1016/j.jcrysgro.2005.11.011> (2006).
23. Kralj, D., Brečević, L. & Kontrec, J. Vaterite growth and dissolution in aqueous solution III. Kinetics of transformation. *J. Cryst. Growth* **177**, 248–257, [https://doi.org/10.1016/S0022-0248\(96\)01128-1](https://doi.org/10.1016/S0022-0248(96)01128-1) (1997).
24. Zhou, G.-T., Yao, Q.-Z., Fu, S.-Q. & Guan, Y.-B. Controlled crystallization of unstable vaterite with distinct morphologies and their polymorphic transition to stable calcite. *Eur. J. Mineral.* **22**, 259–269, <https://doi.org/10.1127/0935-1221/2009/0022-2008> (2010).
25. Shen, Q. *et al.* Properties of Amorphous Calcium Carbonate and the Template Action of Vaterite Spheres. *The. J. Phys. Chem. B* **110**, 2994–3000, <https://doi.org/10.1021/jp055063o> (2006).
26. White, W. B. Thermodynamic equilibrium, kinetics, activation barriers, and reaction mechanisms for chemical reactions in Karst Terrains. *Environ. Geol.* **30**, <https://doi.org/10.1007/s002540050131> (1997).
27. Lioliou, M. G., Paraskeva, C. A., Koutsoukos, P. G. & Payatakes, A. C. Heterogeneous nucleation and growth of calcium carbonate on calcite and quartz. *J. Colloid Interface Sci.* **308**, 421–428, <https://doi.org/10.1016/j.jcis.2006.12.045> (2007).
28. Whiffin, V. S. Microbial CaCO<sub>3</sub> Precipitation for the Production of Biocement. Ph.D. thesis, Murdoch University, Western Australia, <http://researchrepository.murdoch.edu.au/399/2/02Whole.pdf> (2004).
29. Yoneda, J. *et al.* Mechanical behavior of hydrate-bearing pressure-core sediments visualized under triaxial compression. *Mar. Petroleum Geol.* **66**, 451–459, <https://doi.org/10.1016/j.marpetgeo.2015.02.028> (2015).
30. Gonzalez-Muñoz, M., Martinez-Ruiz, F., Morcillo, F., Martin-Ramos, J. & Paytan, A. Precipitation of barite by marine bacteria: A possible mechanism for marine barite formation. *Geology* **40**, 675–678, <https://doi.org/10.1130/G33006.1> (2012).
31. Rodriguez-Blanco, J. D., Shaw, S. & Benning, L. G. How to make ‘stable’ ACC: protocol and preliminary structural characterization. *Mineral. Mag.* **72**, 283–286, <https://doi.org/10.1180/minmag.2008.072.1.283> (2008).
32. Demény, A. *et al.* Formation of amorphous calcium carbonate in caves and its implications for speleothem research. *Sci. Reports* **6**, 39602, <https://doi.org/10.1038/srep39602> (2016).
33. Farhadi-Khouzani, M., Chevrier, D. M., Zhang, P., Hedin, N. & Gebauer, D. Water as the Key to Proto-Aragonite Amorphous CaCO<sub>3</sub>. *Angewandte Chemie - Int. Ed* **55**, 8117–8120, <https://doi.org/10.1002/anie.201603176> (2016).
34. Rodriguez-Navarro, C., Elert, K. & Ševčík, R. Amorphous and crystalline calcium carbonate phases during carbonation of nanolimes: implications in heritage conservation. *CrystEngComm* **18**, 6594–6607, <https://doi.org/10.1039/C6CE01202G> (2016).
35. Krishnamurti, D. The raman spectrum of calcite and its interpretation. *Proc. Indian Acad. Sci. - Sect. A* **46**, 183–202, <https://doi.org/10.1007/BF03045968> (1957).
36. Farsang, S., Facq, S. & Redfern, S. Raman modes of carbonate minerals as pressure and temperature gauges up to 6 GPa and 500 °C. *Am. Mineral.*, <https://doi.org/10.2138/am-2018-6442> (2018).
37. Xu, S. & Wu, P. Monodisperse spherical CaCO<sub>3</sub> superstructure self-assembled by vaterite lamella under control of regenerated silk fibroin via compressed CO<sub>2</sub>. *CrystEngComm* **15**, 5179–5188, <https://doi.org/10.1039/C3CE40181B> (2013).
38. Buczyński, C. & Chafetz, H. S. Habit of bacterially induced precipitates of calcium carbonate and the influence of medium viscosity on mineralogy. *J. Sedimentary Res* **61**, 226–233, <https://doi.org/10.1306/D42676DB-2B26-11D7-8648000102C1865D> (1991).
39. Chekroun, K. B. *et al.* Precipitation and Growth Morphology of Calcium Carbonate Induced by Myxococcus Xanthus: Implications for Recognition of Bacterial Carbonates. *J. Sedimentary Res* **74**, 868–876, <https://doi.org/10.1306/050504740868> (2004).
40. Rautaray, D., Ahmad, A. & Sastry, M. Biosynthesis of CaCO<sub>3</sub> Crystals of Complex Morphology Using a Fungus and an Actinomycete. *J. Am. Chem. Soc.* **125**, 14656–14657, <https://doi.org/10.1021/ja0374877> (2003).
41. Sondi, I. & Matijević, E. Homogeneous precipitation of calcium carbonates by enzyme catalyzed reaction. *J. Colloid Interface Sci* **238**, 208–214, <https://doi.org/10.1006/jcis.2001.7516> (2001).
42. Simmonds, P. G., Medley, E. E., Ratcliff, M. A. & Shulman, G. P. Thermal decomposition of aliphatic monoaminomono carboxylic acids. *Anal. Chem.* **44**, 2060–2066, <https://doi.org/10.1021/ac60320a040> (1972).
43. Jie, L. *et al.* The investigation of thermal decomposition pathways of phenylalanine and tyrosine by TG–FTIR. *Thermochimica Acta* **467**, 20–29, <https://doi.org/10.1016/j.tca.2007.10.014> (2008).
44. Ratcliff, M. A., Medley, E. E. & Simmonds, P. G. Pyrolysis of amino acids. Mechanistic considerations. *The J. Org. Chem.* **39**, 1481–1490, <https://doi.org/10.1021/jo00924a007> (1974).
45. Heveran, C. M. *et al.* Engineered Ureolytic Microorganisms Can Tailor the Morphology and Nanomechanical Properties of Microbial-Precipitated Calcium Carbonate. *Sci. Reports* **9**, 14721, <https://doi.org/10.1038/s41598-019-51133-9> (2019).

46. Rodriguez-Blanco, J. D., Sand, K. K. & Benning, L. G. ACC and Vaterite as Intermediates in the Solution-Based Crystallization of CaCO<sub>3</sub>. In Van Driessche, A. E. S., Kellermeier, M., Benning, L. G. & Gebauer, D. (eds.) *New Perspectives on Mineral Nucleation and Growth: From Solution Precursors to Solid Materials*, 93–111, <https://doi.org/10.1007/978-3-319-45669-0-5> (Springer International Publishing, Cham, 2017).
47. Levi-Kalishman, Y., Raz, S., Weiner, S., Addadi, L. & Sagi, I. X-Ray absorption spectroscopy studies on the structure of a biogenic “amorphous” calcium carbonate phase. *J. Chem. Soc. Dalton Transactions* 3977–3982, <https://doi.org/10.1039/B003242P> (2000).
48. Koga, N. & Yamane, Y. Thermal behaviors of amorphous calcium carbonates prepared in aqueous and ethanol media. *J. Therm. Analysis Calorim.* **94**, 379–387, <https://doi.org/10.1007/s10973-008-9110-3> (2008).
49. Beuvoir, T. *et al.* Synthesis of hollow vaterite CaCO<sub>3</sub> microspheres in supercritical carbon dioxide medium. *J. Mater. Chem.* **21**, 9757–9761, <https://doi.org/10.1039/C1JM10770D> (2011).
50. Takahashi, K. *et al.* Formation of 6-, 7- or 8-membered ring intra-side-chain NHO hydrogen bond toward Ca-binding oxyanion in poly(allylaminocarboxylate) ligands stabilizes CaCO<sub>3</sub> vaterite crystals. *J. Cryst. Growth* **263**, 552–563, <https://doi.org/10.1016/j.jcrysgro.2003.11.112> (2004).
51. Ueyama, N., Takahashi, K., Onoda, A., Okamura, T.-A. & Yamamoto, H. Tight binding of poly(carboxylate) ligand to calcium carbonate with intramolecular NH...O hydrogen bond. *Macromol. Symp.* **186**, 129–134, [https://doi.org/10.1002/1521-3900\(200208\)186:1<129::AID-MASY129>3.0.CO;2-F](https://doi.org/10.1002/1521-3900(200208)186:1<129::AID-MASY129>3.0.CO;2-F) (2002).
52. Štajner, L. *et al.* The effect of different amino acids on spontaneous precipitation of calcium carbonate polymorphs. *J. Cryst. Growth* **486**, 71–81, <https://doi.org/10.1016/j.jcrysgro.2018.01.023> (2018).
53. Aizenberg, J., Addadi, L., Weiner, S. & Lambert, G. Stabilization of amorphous calcium carbonate by specialized macromolecules in biological and synthetic precipitates. *Adv. Mater.* **8**, 222–226, <https://doi.org/10.1002/adma.19960080307> (1996).
54. Jaenicke, R. & Bohm, G. The stability of proteins in extreme environments. *Current opinion in structural biology. Curr. Opin. Struct. Biol.* **8**, 738–748 (1998).
55. Razvi, A. & Scholtz, J. M. Lessons in stability from thermophilic proteins. *Protein Sci.* **15**, 1569–1578, <https://doi.org/10.1110/ps.062130306> (2006).
56. Matsumura, P., Keller, D. M. & Marquis, R. E. Restricted pH ranges and reduced yields for bacterial growth under pressure. *Microb. Ecol.* **1**, 176–189, <https://doi.org/10.1007/BF02512388> (1974).
57. Kaneshiro, S. M. & Clark, D. S. Pressure effects on the composition and thermal behavior of lipids from the deep-sea thermophile *Methanococcus jannaschii*. *J. Bacteriol.* **177**, 3668–3672, <https://doi.org/10.1128/jb.177.13.3668-3672.1995> (1995).
58. Kumar, P. & Libchaber, A. Pressure and Temperature Dependence of Growth and Morphology of *Escherichia coli*: Experiments and Stochastic Model. *Biophys. J.* **105**, 783–793, <https://doi.org/10.1016/j.bpj.2013.06.029> (2013).
59. Yang, P., O'Donnell, S., Hamdan, N., Kavazanjian, E. & Neithalath, N. 3D DEM Simulations of Drained Triaxial Compression of Sand Strengthened Using Microbially Induced Carbonate Precipitation. *Int. J. Geomech.* **17**, 04016143, [https://doi.org/10.1061/\(ASCE\)GM.1943-5622.0000848](https://doi.org/10.1061/(ASCE)GM.1943-5622.0000848) (2017).
60. Feng, K., Montoya, B. M. & Evans, T. M. Discrete element method simulations of bio-cemented sands. *Comput. Geotech.* **85**, 139–150, <https://doi.org/10.1016/j.compgeo.2016.12.028> (2017).
61. Yang, Z. X., Yang, J. & Wang, L. Z. On the influence of inter-particle friction and dilatancy in granular materials: a numerical analysis. *Granul. Matter* **14**, 433–447, <https://doi.org/10.1007/s10035-012-0348-x> (2012).
62. SigmaPlot. PeakFit - The Automatic Choice for Spectroscopy, Chromatography and Electrophoresis.
63. Saloman, E. B. & Sansonetti, C. J. Wavelengths, Energy Level Classifications, and Energy Levels for the Spectrum of Neutral Neon. *J. Phys. Chem. Ref. Data* **33**, 1113–1158, <https://doi.org/10.1063/1.1797771> (2004).
64. EVA (Bruker). DIFFRAC.SUITE EVA.

## Acknowledgements

The authors would like to thank John Chandler, Kristian Pether, Mark Smith, and Chris McGinnie for facilitating the experiments; Dr Giulio I. Lampronti and Len Howlett for their assistance with XRD and SEM analysis, respectively; Dr Stuart Scott for lending the TGA-MS equipment; and Dr Rod Lynch for reviewing the manuscript. The authors would also like to acknowledge the EPSRC Centre for Doctoral Training in Future Infrastructure and Built Environment at the University of Cambridge (EPSRC grant reference number EP/L016095/1). This study was conducted as part of the activity of the Research Consortium for Methane Hydrate Resources in Japan [MH21 Research Consortium] as planned by the Ministry of Economy, Trade, and Industry (METI), Japan. We would like to express our sincere thanks to the crew of D/V Chikyu for the 2012 JOGMEC/JAPEX pressure coring operation.

## Author contributions

A.C.S., S.K.H. and T.H. conceived experimental program. T.H. isolated *S. newyorkensis*. A.C.S. and T.H. cultivated the three bacterial strains, performed *in vitro* precipitation, and monitored chemical evolution. S.A.T.R. advised on the Raman spectroscopy collection program and data interpretation. A.C.S. and S.F. collected the Raman spectra, and analysed and interpreted the results. E.M. conducted MS analyses and helped A.C.S. with the acquisition and interpretation of TG-MS results. A.C.S. performed the XRD analyses and SEM images. T.H. planned and performed the pressure-temperature cultivation experiments, and A.C.S. analysed and interpreted the results. K.S. facilitated the collaboration between A.C.S., S.K.H., and T.H. A.C.S. coordinated the collaboration and wrote the manuscript with the help of co-authors. All authors reviewed the manuscript.

## Competing interests

The authors declare no competing interests.

## Additional information

**Supplementary information** is available for this paper at <https://doi.org/10.1038/s41598-020-66831-y>.

**Correspondence** and requests for materials should be addressed to A.C.S.

**Reprints and permissions information** is available at [www.nature.com/reprints](http://www.nature.com/reprints).

**Publisher's note** Springer Nature remains neutral with regard to jurisdictional claims in published maps and institutional affiliations.



**Open Access** This article is licensed under a Creative Commons Attribution 4.0 International License, which permits use, sharing, adaptation, distribution and reproduction in any medium or format, as long as you give appropriate credit to the original author(s) and the source, provide a link to the Creative Commons license, and indicate if changes were made. The images or other third party material in this article are included in the article's Creative Commons license, unless indicated otherwise in a credit line to the material. If material is not included in the article's Creative Commons license and your intended use is not permitted by statutory regulation or exceeds the permitted use, you will need to obtain permission directly from the copyright holder. To view a copy of this license, visit <http://creativecommons.org/licenses/by/4.0/>.

© The Author(s) 2020